Climate Dynamics (2026) 64:48
https://doi.org/10.1007/s00382-025-08025-8

Diurnal variation of summer precipitation in the middle and lower Yangtze River Basin and associated mechanisms

Xueqing Yuan[1] · Anning Huang[1] · Guangtao Dong[2] · Daokai Xue[1] · Xinsheng Zhu[3] · Rongchang Wu[1]

Received: 8 February 2025 / Accepted: 17 December 2025

Abstract

Precipitation diurnal variation is crucial for understanding the precipitation processes and improving the forecast skill of precipitation. In this study, the detailed features of precipitation diurnal variation over the middle and lower Yangtze River Basin in summer and associated mechanisms have been systematically revealed based on the high-resolution observational and reanalysis data of 1980 to 2022. The results show that the precipitation diurnal variation exhibits a distinct bimodal feature, with a primary peak occurring at 16:00–18:00 Beijing time (BJT) and a secondary peak concentrated around 07:00–09:00 BJT. Composite analysis of the three precipitation-day types (morning peak, afternoon peak, and dual-peak) reveals their fundamentally different environmental configurations: the morning type is dominated by nocturnal large-scale dynamic lifting that consumes pre-stored moisture; the afternoon type is governed by local thermal processes relying on daytime surface evaporation and energy storage; while the dual-peak type reflects the synergistic effect between dynamic forcing and thermal processes, with its morning peak driven by persistent dynamic convergence and its afternoon peak formed by thermal lifting that releases morning-accumulated energy. Spatially, cluster analysis identifies four characteristic patterns of precipitation diurnal variation: northwestern morning-dominant, mountainous afternoon-enhanced, transitional bimodal equilibrium, and southeastern coastal afternoon-dominant patterns. The differences among these patterns are primarily reflected in the afternoon peak precipitation (dominated by short- and medium-duration events). The spatial heterogeneity is primarily governed by thermally forced ascent: differential heating (mountain-plain and land-sea contrasts) generates upward motion, which is then intensified by topographic lifting, leading to strongly enhanced ascent and consequently higher afternoon precipitation in mountainous and coastal hilly areas. Furthermore, the study documents a distinct southeastward propagation delay of morning precipitation peaks within the 110°E–119°E and 28°N–30°N range, expanding understanding beyond the traditional paradigm of limited eastward propagation of morning precipitation. Sub-seasonal variation of the precipitation diurnal cycle shows a morning-to-afternoon transition, shifting from large-scale moisture transport dominance during the pre-Meiyu and Meiyu periods to thermal instability dominance in the post-Meiyu period.

Keywords The middle and lower Yangtze River Basin · Diurnal variation of precipitation · Summer · Regional differences · Sub-seasonal differences

1 Introduction

Precipitation connects the atmosphere, land, and oceans across regional and global scales, playing a crucial role in energy exchange and climate regulation (Held and Soden 2006; Oki and Kanae 2006; Rodell et al. 2018; Trenberth et al. 2007). The intensity, frequency, and duration of precipitation events are largely affected by climate change (Hansen et al. 2012; Meehl et al. 2000; Trenberth et al. 2003; Xiao et al. 2016; Zhang et al. 2021). Important information on changes in precipitation frequency and intensity can be obtained by meticulously investigating the timing and

✉ Anning Huang
anhuang@nju.edu.cn

✉ Xinsheng Zhu
zxs_dream@yeah.net

[1] School of Atmospheric Sciences, Nanjing University, Nanjing 210023, China

[2] Shanghai Climate Center, Shanghai 200030, China

[3] Nanjing Institute of Environmental Sciences, Ministry of Ecology and Environment of the People's Republic of China, Nanjing 210033, China

Published online: 13 January 2026

duration of precipitation (Liu et al. 2024; Lu et al. 2017; Trenberth et al. 2003; Zhou et al. 2008). However, due to the limitations of model simulations in accurately capturing the diurnal variations of precipitation, such as discrepancies in peak times and precipitation during peak periods (Jiang et al. 2024; Jin et al. 2016; Li et al. 2023; Niu et al. 2020; Shi et al. 2024; Yu et al. 2014), it is necessary to analyze the precipitation data at sub-daily scale to comprehend better the underlying physical mechanism related to the diurnal variation of precipitation and address these shortcomings.

Situated in a typical monsoon climate zone, the rainy season in the middle and lower Yangtze River Basin (MLYRB) is concentrated in the summer months. The summer precipitation in this region is shaped by the complex interactions of the western Pacific subtropical high, the East Asian monsoon, typhoons, various weather systems, different surface types, and terrains, resulting in distinctive precipitation patterns (Bao et al. 2011; Geng and Yamada 2007; Xuan et al. 2018; Xue et al. 2018; Yuan et al. 2010; Zhang 2022; Zhao et al. 2016). Because of its highly developed economy and dense population, the MLYRB is especially susceptible to catastrophic precipitation events like droughts and floods, which pose significant risks to agriculture, transportation, and urban infrastructure (Hu et al. 2019; Tang et al. 2021). For instance, the unprecedented 2020 Meiyu, characterized by record-high cumulative precipitation and duration since 1961, resulted in severe flooding (Zhou et al. 2021). Furthermore, the MLYRB features a complex topography, primarily composed of alluvial plains, interspersed with hills and mountains (Fig. 1b). The interplay of this topography

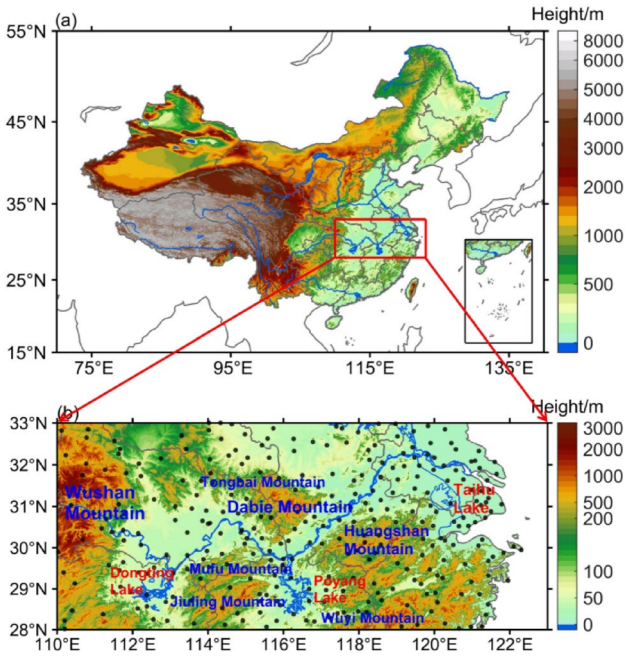

Fig. 1 The spatial distribution of terrain in China (**a**) and the distribution of rain gauge stations and terrain in the MLYRB (**b**)

with the monsoon climate amplifies the diurnal variance in precipitation. Given the region's socio-economic significance, selecting the MLYRB as a study area is not only scientifically important, but it also provides practical insights for disaster prevention, mitigation, and water resource management.

Numerous studies have demonstrated that summer precipitation in East Asia exhibits significant diurnal variation, with noteworthy regional and sub-seasonal differences. Specifically, the precipitation diurnal peaks around midnight in the eastern Tibetan Plateau and Sichuan Basin, reaches a morning peak in the middle Yangtze River, and follows double peaks with one in the early morning and the other in the afternoon over eastern China (Bao et al. 2011; Liu et al. 2021; Wu et al. 2018; Yin et al. 2009; Yu et al. 2014, 2007a, b; Zhou et al. 2008; Zhu et al. 2018). Additionally, the sub-seasonal evolution of precipitation diurnal variation is closely linked to the migration of the East Asian monsoon rain belt (Bao et al. 2011; Geng and Yamada 2007; Yuan et al. 2010). The diurnal variation of long-duration precipitation over the regions east of the Tibetan Plateau is clearly marked by an eastward-delayed diurnal phase during the active monsoon season (Chen et al. 2012, 2010, 2009a; Huang and Wang 2017; Wu et al. 2018; Yuan et al. 2010; Zhu et al. 2023).

Furthermore, researchers suggest that the air thermal instability caused by solar radiation heating is the primary source of the afternoon precipitation diurnal peak. On the other hand, the strengthened transport of water vapor which is powered by both regional mountain-valley wind circulations and nocturnal accelerated low-level winds is responsible for the night/early morning peak (Fu et al. 2019; Geng et al. 2009; He et al. 2016; Li et al. 2024; Singh and Nakamura 2009; Xue et al. 2018; Yin et al. 2009; Yu et al. 2007b; Yuan et al. 2012b).

Despite significant progress in research on precipitation diurnal variations in the East Asian monsoon region, current studies still face two critical data limitations: First, traditional studies based on low-density station networks struggle to capture the refined spatial heterogeneity of diurnal precipitation variations (Chen et al. 2009b); Second, alternative data sources (satellite remote sensing and reanalysis products) exhibit unavoidable systematic biases (Chen et al. 2018, 2016; Hur et al. 2018; Li et al. 2018; Mao and Wu 2012; Qian et al. 2015; Tang et al. 2020; Zhu et al. 2023). These manifest specifically as: (1) Satellite products usually misrepresent diurnal precipitation characteristics—failing to capture the morning peak in the Yangtze region while reversing the observed bimodal structure to an afternoon-dominant pattern in the Huaihe Basin (Zhu et al. 2018), with particularly pronounced underestimation of morning precipitation and overestimation of afternoon precipitation

during Meiyu season (Chen et al. 2016; Shen et al. 2010; Yuan et al. 2012a); (2) Reanalysis data typically underestimate the amplitude of diurnal precipitation variation but overestimate the daytime precipitation (Dai et al. 2011; Qin et al. 2021). These limitations highlight the necessity of employing high-density networks of direct observation for refined research.

Based on the hourly rain gauge data in the summers (June to August) of 1980 to 2022 from 300 stations which are densely and nearly evenly distributed across the MLYRB, this study will answer such questions as follows: What are the differences in environmental conditions among different regional diurnal precipitation regimes? What fine-scale spatial heterogeneity does the diurnal variation of summer precipitation exhibit over the MLYRB, and what are the underlying causes? How does the dynamical competition between large-scale moisture transport and thermal forcing govern the sub-seasonal evolution of the dominant diurnal phase of precipitation? The findings of this study may contribute to deepening the understanding of the diurnal variation characteristics of summer precipitation in the MLYRB and provide essential references for evaluating and improving numerical models, as well as enhancing the accuracy of refined precipitation forecasts.

2 Data and methods

2.1 Data

The China Meteorological Administration (CMA) provides hourly rain gauge precipitation data from 300 stations in the MLYRB region throughout the summer months (June to August) of 1980 to 2022 (Fig. 1). The missing data rate at each station is less than 3%, with missing precipitation values filled by interpolate the data from nearby stations (Zeng et al. 2023). Additional meteorological variables, including specific humidity, precipitable water, evaporation, convective available potential energy (CAPE), and zonal and meridional wind components are obtained from the ERA5 reanalysis dataset with a spatial resolution of 0.25° and a temporal resolution of 1 h (Hersbach et al. 2020).

2.2 Methods

2.2.1 Definition of precipitation amount, frequency and intensity

Referring to Yu et al. (2007b) and Zhou et al. (2008), the metrics of precipitation amount (PA), frequency (PF), and intensity (PI) are introduced to characterize precipitation. If the precipitation in a given rain gauge station at a given hour is greater than or equal to 0.1 mm, then this hour is detected as a precipitation hour for this rain gauge station. The climatic mean summer PA, PF, and PI during 1980–2022 at each station for each hour of a day are calculated as follows: for a given station, the PA (PF) at a given hour of a day is firstly calculated as the total rainfall (total precipitation hours multiplied by 100%) in the summers of 1980–2022 at this hour divided by the total hours, which equal 92 h/year × 43 years. Then we can get PI, which equals PA/PF at a given rain gauge station for each hour of the day. The units of PA and PI (PF) are mm/h (100%).

2.2.2 Single-station precipitation event

Precipitation events are extracted from the hourly rain gauge data, with the hours having precipitation amount ≥ 0.1 mm classified as precipitation hours (Wu et al. 2018). Consecutive precipitation hours are grouped into a single precipitation process, and a precipitation process occurring at a single station is defined as a precipitation event at that station.

The total number of hours from the start to the end of a precipitation event is known as its duration (Yu et al. 2007a). To compare the features of diurnal variation in precipitation events with different duration, following the method of Liu et al. (2021), the precipitation events are classified into three categories: short-duration events which last up to 3 h (≤ 3 h), medium-duration events which last 4–5 h, and long-duration events which last more than 6 h (> 6 h). In Sect. 3.1, when discussing the precipitation events of varying duration, the peak time of precipitation events refers to the moment when the maximum precipitation intensity occurs during each precipitation event. Additionally, for the calculation of PA, PF, and PI across different durations, we isolated the relevant precipitation events by filtering the complete time series based on duration-specific criteria, which effectively removes the influence of non-rainy hours.

2.2.3 Definition of regional rainy day

To investigate the environmental conditions associated with different diurnal regimes of precipitation over the MLYRB in summer, this study established a regional rainy day identification criterion following the methodology of Song and Wei (2021): a regional rainy day is detected when the regional mean precipitation over the MLYRB at least one hour exceeds 0.1 mm in a given day. Based on the diurnal peak of PA in the MLYRB, regional precipitation days are categorized into three categories using a relative threshold of 1.5, with morning hours defined as 00:00–11:00 BJT and afternoon hours as 12:00–23:00 BJT: (1) morning precipitation days (morning-to-afternoon peak ratio > 1.5), (2) afternoon precipitation days (afternoon-to-morning peak

ratio > 1.5), and (3) dual-peak precipitation days (peak ratio between 1/1.5 and 1.5). Sensitivity tests demonstrated that the key moisture, dynamic, and thermodynamic characteristics of both precipitation types remain robust under different time window selections. Therefore, a wide time window was adopted to include more sample days.

2.2.4 Spectral clustering analysis methods

Spectral clustering is a graph-based method used to partition a dataset into multiple clusters. The basic idea involves performing spectral decomposition on the similarity matrix of the data, which maps the data into a lower-dimensional space. Traditional clustering algorithms are then applied in this lower-dimensional space. Spectral clustering frequently performs better than traditional clustering techniques like K-means clustering, particularly when the number of clusters is small (Ng et al. 2001; Shi and Malik 2000; von Luxburg 2007).

The spectral clustering analysis utilized in this study for the PA consists of four steps (Chen et al. 2010):

1. Normalization: First, the diurnal variation time series of the climatic mean PA for each station in the MLYRB are calculated at each hour of a day. To better reflect the diurnal variation trends of these precipitation indices, the series are normalized as follows:

$$D_t = \frac{R_t}{\frac{1}{24}\sum_{t=0}^{23} R_t} \tag{1}$$

D_t represents the normalized PA at the *t*th hour of a day, and R_t denote the climatic mean of PA (or PF, PI) at the *t*th hour of a day.

2. Harmonic Analysis: The normalized diurnal variation time series of PA are subjected to harmonic analysis using the Fourier method. Given that the period of harmonics related to diurnal variation is always equal to or less than 24 h, 24 h is selected as the fundamental period. Various periodic harmonics are decomposed, where $m = 1$ corresponds to the 24-h harmonic (diurnal cycle), $m = 2$ corresponds to the 12-h harmonic (semi-diurnal cycle), and $m = 3$ corresponds to the 8-h harmonic. Prior research has demonstrated that the diurnal and semi-diurnal cycles are the main signals of diurnal variation in precipitation (Tucker 1993; Watters and Battaglia 2019). Therefore, in this study, the first three harmonics ($m = 1, 2, 3$) are used to approximate the original time series, smoothing the series while retaining its original fluctuation characteristics:

$$D_t = \overline{D} + \sum_{m=1}^{3}\left(a_k cos\frac{m\pi t}{24} + b_k sin\frac{m\pi t}{24}\right) + R \tag{2}$$

$$\overline{D} = \frac{1}{24}\sum_{t=0}^{23} D_t \tag{3}$$

D_t represents the normalized PA (or PF, PI) at the t^{th} hour of a day, $\overline{D}$ represents the daily mean of D_t, $m = 1, 2, 3$ correspond to the harmonics with periods of 24h, 12h, and 8h, respectively, and R represents the residual term, capturing all harmonics with periods shorter than 8h.

3. Significance Testing: An F-test is conducted to exclude stations where none of the first three harmonics are statistically significant at the 0.05 level, thereby ensuring the robustness of the harmonic analysis results.

4. Spectral Clustering Analysis: Spectral clustering analysis is performed on the harmonic series of PA. Based on the Calinski-Harabasz score (Calinski and Harabasz 1974), we identified four typical patterns of the PA diurnal variation in summer over the MLYRB. Then, the PA is regionally averaged over the stations within the same pattern to derive the characteristics of PA diurnal variation for each typical pattern.

2.2.5 Moisture budget analysis

The moisture sources and budget processes governing the diurnal cycle of precipitation are diagnosed using the atmospheric moisture budget equation, following the framework of Trenberth (1991). In this study, the equation is formulated to isolate precipitation as the key diagnostic variable:

$$P = E - \partial W/\partial t - \nabla \cdot \overrightarrow{Q} \tag{4}$$

Here, P is the precipitation rate, E is the surface evaporation rate, W is the precipitable water (vertically integrated water vapor), defined as $W = \frac{1}{g}\int_{Pt}^{Ps} q dp$, and $\overrightarrow{Q}$ is the vertically integrated horizontal moisture flux, defined as $\overrightarrow{Q} = \int_{P_t}^{P_s} q\overrightarrow{V}\,dp$, where P_s denotes the surface pressure and P_t denotes the pressure at the top of the atmosphere. Given that atmospheric moisture is predominantly concentrated within the troposphere, the integration top P_t in this study is set to 100 hPa to ensure the capture of the vast majority of the moisture signal. The term $-\partial W/\partial t$ represents the contribution from the depletion of locally stored atmospheric moisture, meaning that a decline in precipitable water over time directly contributes to the rainfall amount.

The term $-\nabla \cdot \overrightarrow{Q}$ represents the moisture flux convergence (MFC). To elucidate the underlying dynamics, this convergence term is decomposed into its dynamic and thermodynamic components:

$$-\nabla \cdot \overrightarrow{Q} = -\nabla \cdot (q\overrightarrow{V}) = (-q\nabla \cdot \overrightarrow{V}) + (-\overrightarrow{V} \cdot \nabla q) \tag{5}$$

Thus, the moisture flux convergence term is separated into the wind convergence term ($-q\nabla \cdot \vec{V}$) and the moisture advection term ($-\vec{V} \cdot \nabla q$).

3 Results

3.1 Features of precipitation diurnal variation over the MLYRB in summer

Figure 2 reveals a distinct bimodal structure in the diurnal variation of summer precipitation over the MLYRB, characterized by dual peaks occurring at 07:00–09:00 BJT and 16:00–18:00 BJT. In terms of PF, two comparable peaks are observed around 07:00 BJT and 17:00 BJT (Fig. 2b). Meanwhile, PI exhibits slightly higher values during the afternoon than in the morning (Fig. 2c), contributing to a more prominent afternoon peak in PA (Fig. 2a).

Analysis of precipitation types indicates that the morning PA peak is predominantly driven by long-duration precipitation, which also accounts for the maximum PF (6.7%) and high PI (3.3 mm/h) around 08:00 BJT. In contrast, the afternoon peak is dominated by short-duration precipitation, which achieves synchronized maxima in both PF (4.7%) and PI (2.4 mm/h) at 17:00 BJT, resulting in a notable synergistic enhancement effect.

The diurnal phase differences are further elucidated through precipitation timing characteristics. Short-duration precipitation exhibits distinct afternoon initiation and peak timing (15:00–18:00 BJT), while long-duration precipitation features nocturnal initiation (23:00–04:00 BJT) and stable morning peak timing (06:00–10:00 BJT). Moreover, although the start time of long-duration precipitation advances and the end time delays with increasing duration, its peak time remains consistently stable at 06:00–10:00 BJT. These features confirm that short- and long-duration precipitation govern the distinct characteristics of the afternoon and morning diurnal peaks, respectively.

The temporally differentiated mechanisms dominated by precipitation duration further determine the spatial distribution patterns of both regional precipitation and its diurnal variation. The PA values at most stations of the MLYRB during nighttime are below the daily mean (Fig. 3a, b, g, and h). During the early morning, although most stations exhibit positive PA anomalies, the northwestern Wushan region and southeastern coastal areas still show negative PA anomalies (Fig. 3c, d). Notably, in the afternoon, the PA increases significantly in the southeastern MLYRB, particularly in the central mountainous areas and their surrounding regions, as well as in the southeastern coastal hilly areas (Fig. 3e, f).

Figure 4 displays the spatial distribution of the PA, PF, and PI for the total, short-, medium-, and long-duration precipitation over the MLYRB in summer. For the total precipitation, there are two primary centers of high PA: one is located in the Huangshan and Dabie Mountains region, and the other is situated in the southeastern coastal area (Fig. 4a). As shown in Fig. 4d, the overall distribution of PF for the total precipitation shows a gradual increase from northwest to southeast, with significantly higher PF in the southeast coastal hilly areas and the mountainous regions

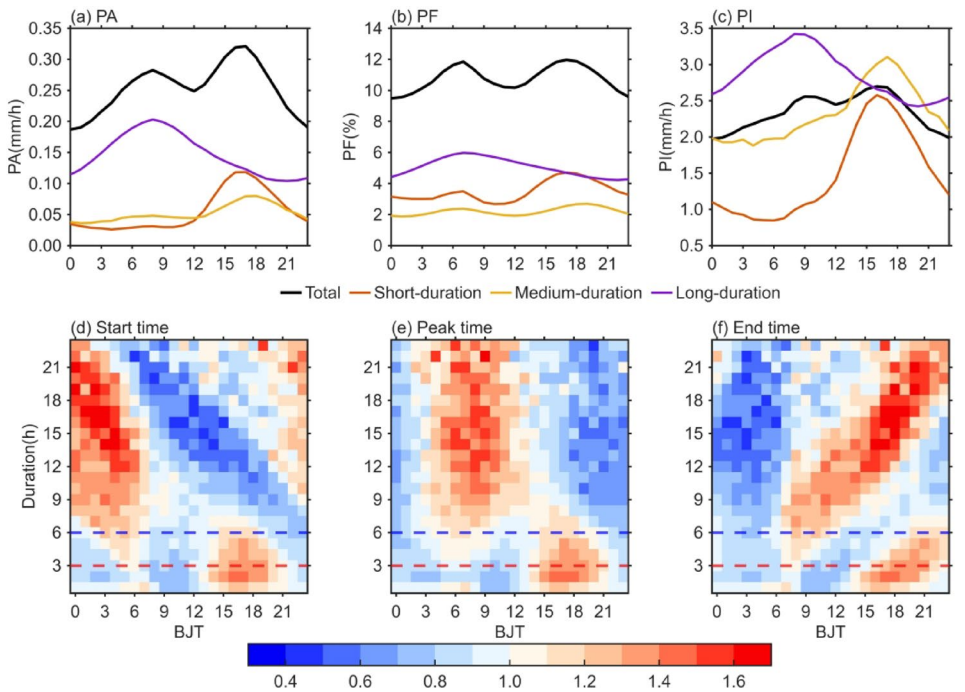

Fig. 2 Climatic mean diurnal variations of (**a**) PA, (**b**) PF, and (**c**) PI for total, short-, medium-, and long-duration precipitation; and normalized occurrence frequency of start time (**d**), peak time (**e**), and end time (**f**) for precipitation events with different durations regionally averaged over the MLYRB during summer from 1980 to 2022. All frequency values are normalized by the daily mean

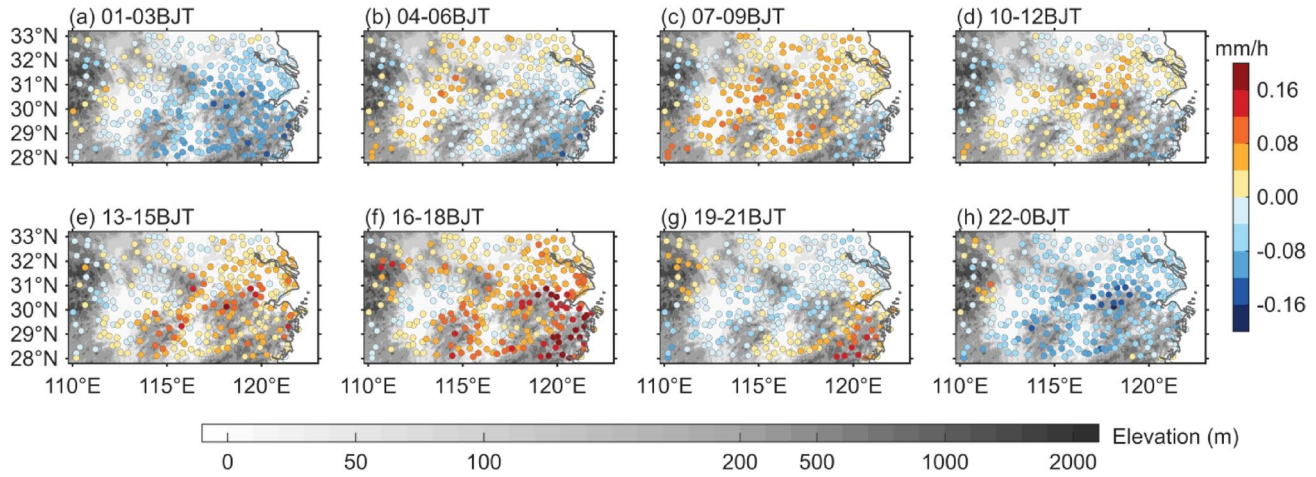

Fig. 3 Spatial distribution of the PA anomalies (relative to the daily mean) at 3-h intervals over the MLYRB in summer averaged over 1980–2022

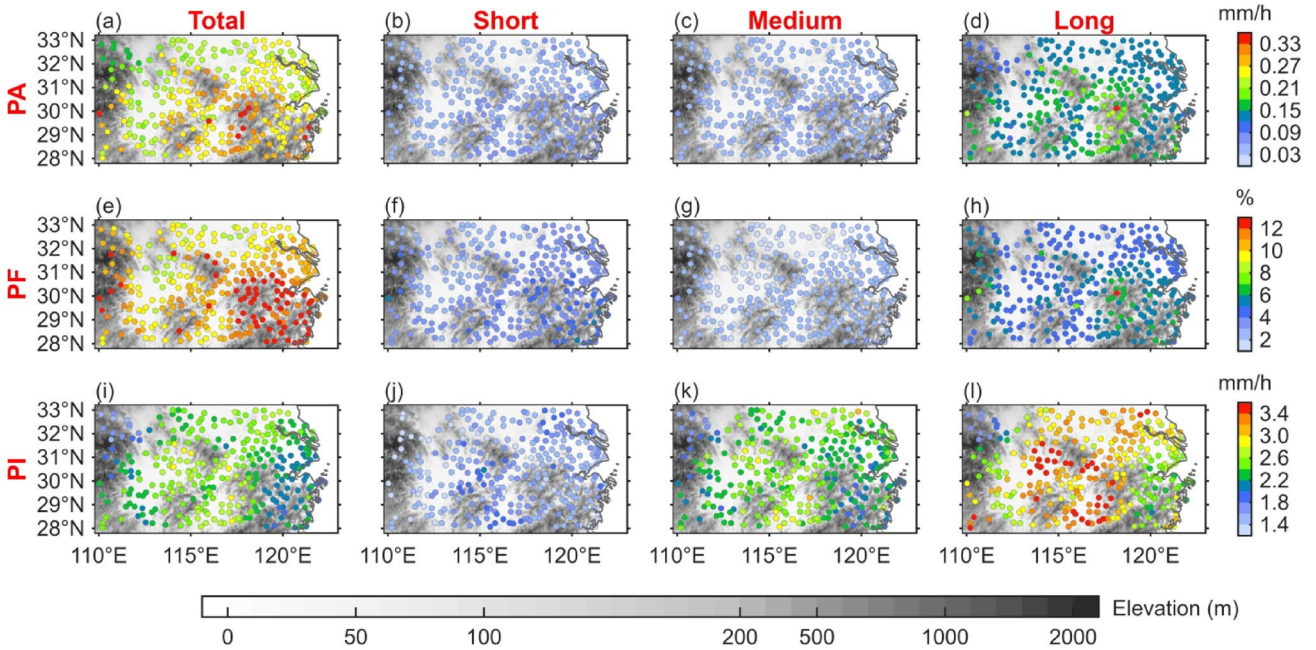

Fig. 4 Spatial distribution of PA (**a**–**d**), PF (**e**–**h**), and PI (**i**–**l**) for the total, short-, medium-, and long-duration precipitation in the MLYRB during summer averaged over 1980–2022

with relatively higher elevations compared to the other areas. From Fig. 4g, a relatively higher PI of total precipitation is located in the plain and lake areas, particularly in the regions nestled between the Dabie, Huangshan, Mufu, and Jiuling Mountains, where the PI is stronger than 2.8 mm/h. This may be related to the eastward movement and intensification of the mesoscale convective systems (MCSs), which originate from the second-step terrain (Yang et al. 2020).

Overall, the high PA in the southeast coastal hilly areas can be attributed to the high PF there, while the high PA in the Huangshan and Dabie Mountains is primarily due to both high PF and PI. Compared to the short- and medium-duration precipitation (Fig. 4b, c, f, g, j, k), the long-duration precipitation shows much higher PA, PF, and PI in almost the entire MLYRB (Fig. 4d, h, and i), leading to the spatial distribution of PA, PF, and PI of long-duration precipitation closely resembling that of total precipitation (Fig. 4a, e, i).

3.2 Environmental configurations of three regional diurnal precipitation regimes

We identified 666 morning precipitation days, 1042 afternoon precipitation days, and 1,080 dual-peak precipitation days during the summers of 1980–2022 (Fig. 5a–d). In terms of spatial patterns, both morning-type and dual-peak precipitation exhibit concentrated precipitation maxima

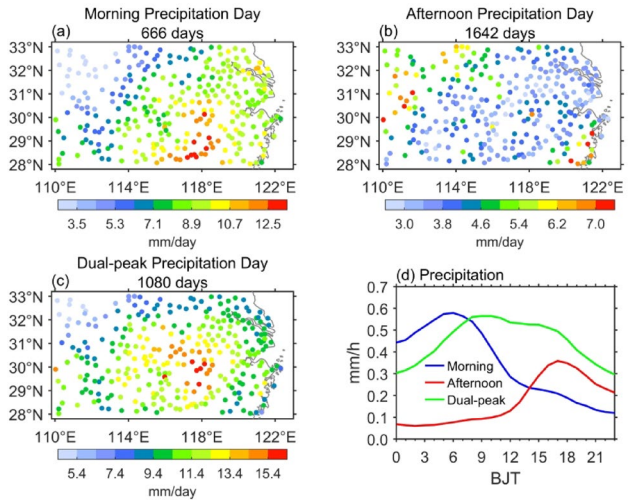

Fig. 5 Spatial distributions of composite mean precipitation (**a**–**c**) and diurnal variations of precipitation (**d**) for morning, afternoon, and dual-peak precipitation days. All analyses are calculated exclusively from their respective precipitation day categories

in the central mountainous region, with the morning-type shifted southward and the dual-peak type shifted northward (Fig. 5a, c). In contrast, afternoon-type precipitation shows a multi-center distribution pattern, mainly occurring in the southeastern hilly areas and the central-western mountainous regions above 500 m elevation (Fig. 5b). Motivated by these distinct spatiotemporal characteristics, this study aims to elucidate the key environmental distinctions among the three precipitation categories by systematically diagnosing their moisture conditions, vertical motion, and instability energy.

For morning precipitation days, moisture conditions show typical "nocturnal convergence-daytime divergence" and "storage consumption" characteristics. The MFC term $(-\nabla \cdot \vec{Q})$ exhibits convergence during nighttime to early morning (00:00–11:00 BJT), peaking around 06:00 BJT with an intensity of 0.26 mm/h, while turning to divergence during afternoon to nighttime (12:00–23:00 BJT), indicating the large-scale dynamic lifting mechanism driving precipitation has strong diurnal variation, mainly active at night (Fig. 6a). Meanwhile, the local moisture change term $(-\partial W/\partial t)$ remains positive almost throughout the day, indicating continuous consumption of total precipitable water, with the fastest consumption during early morning and evening hours (Fig. 6c). Peak consumption rates occur at 05:00 BJT and 18:00 BJT, reaching 0.28 mm/h and 0.36 mm/h (Fig. 6c), respectively, indicating this precipitation type mainly relies on consuming existing atmospheric moisture reserves rather than sustained strong convergence supply. In terms of thermal conditions, CAPE values remain at relatively low levels throughout the day (below 600 J/kg) (Fig. 6g), with generally stable atmospheric stratification. The vertical velocity field (Fig. 6g) shows exhibits consistent upward motion from 900 hPa to the tropopause during the morning precipitation peak, with the maximum ascent center located at 400–600 hPa, reaching a value of −0.11 Pa/s. Notably, from afternoon onward, the mid-low layers gradually transition to subsidence, with complete subsidence below 600 hPa by 18:00 BJT. This configuration indicates the morning precipitation peak is mainly driven by nocturnally enhanced large-scale dynamic lifting mechanisms (like the low-level jet) utilizing pre-stored moisture. During the daytime, as moisture flux conditions become divergent, convection is suppressed despite evaporation, resulting in a sharp decrease in precipitation.

In stark contrast, afternoon precipitation days exhibit "persistent convergence" and "storage-release" moisture patterns. Although MFC persists almost throughout the day, the intensity is weak, with a daily mean of only 0.09 mm/h (Fig. 6a), and moisture flux from the southwest is significantly weaker than the climatic mean (Fig. 6e). The key feature of the local moisture change term is the consistently negative $-\partial W/\partial t$ during 06:00–16:00 BJT, indicating continuous increase in local atmospheric moisture content, turning to weak consumption after 16:00 BJT (Fig. 6c), meaning converged moisture is not immediately consumed but largely stored, increasing atmospheric instability energy. Combined with the strongest surface evaporation among the three types (Fig. 6b), daytime thermal effects provide ample local moisture to the atmosphere. Regarding thermal conditions, CAPE shows significant diurnal variation, with afternoon peaks exceeding 1200 J/kg, accumulating sufficient instability energy in the atmosphere (Fig. 6h). During the peak CAPE period, the vertical velocity field exhibits deep upward motion extending from the surface to 100 hPa. Although the intensity is relatively weak (maximum ascent of approximately -0.06 Pa/s), it still demonstrates structural characteristics of deep convection (Fig. 6h). Overall, thermal driving likely dominates this precipitation type formation, where weak dynamic convergence and strong evaporation jointly "recharge" the atmosphere. When afternoon thermal instability peaks, stored moisture is rapidly released, generating sharp afternoon precipitation peaks.

Finally, dual-peak precipitation days exhibit "strong convergence" and "semi-diurnal cycle" configurations. The MFC term shows persistently strong convergence (Fig. 6a), with a daily mean intensity of 0.27 mm/h, and morning convergence intensity is significantly higher than afternoon (Fig. 6a). The sustained strong MFC corresponds to the robust quasi-southwest-northeast large-scale dynamic system indicated in Fig. 6f, providing continuous moisture supply for precipitation. Their moisture content variation shows a clear semi-diurnal cycle: 07:00–14:00 BJT is the

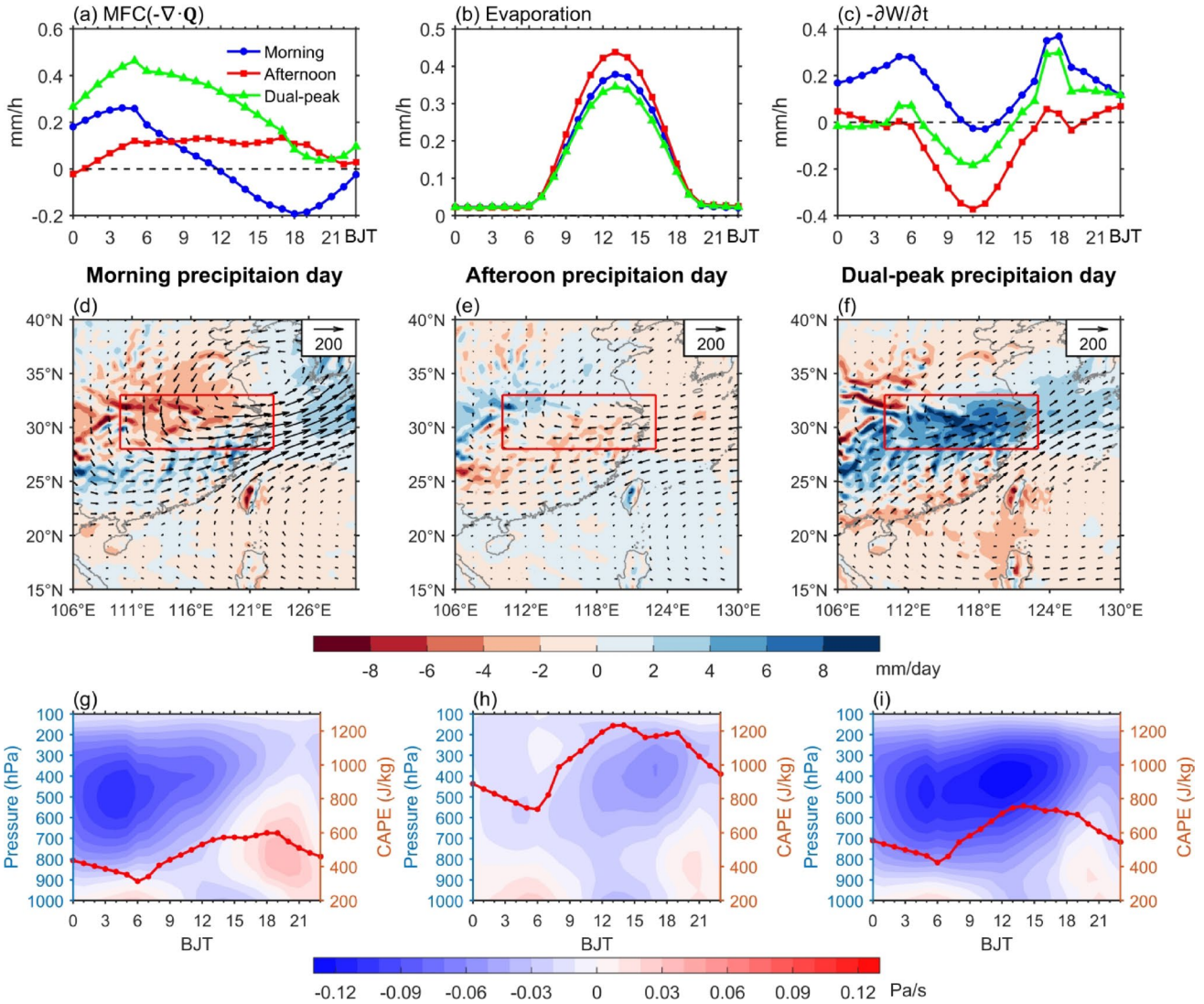

Fig. 6 Diurnal variations of regionally averaged (over the MLYRB) MFC ($-\nabla \cdot \vec{Q}$) (**a**), evaporation (**b**), and precipitable water tendency ($-\partial W/\partial t$) (**c**) for different precipitation day types (units: mm/h). Anomalies of column-integrated (surface to 100 hPa) moisture flux (vectors, kg m^{-1} s^{-1}) and its convergence (MFC, shading, mm/day) for morning (**d**), afternoon (**e**), and dual-peak (**f**) precipitation days. Diurnal variations of regionally averaged vertical velocity (shading, Pa/s) and CAPE (red line, J/kg) for morning (**g**), afternoon (**h**), and dual-peak (**i**) precipitation days. All analyses are calculated exclusively from their respective precipitation day categories, and all anomalies represent deviations relative to the 1980–2022 climatic mean

moisture accumulation phase ($-\partial W/\partial t<0$); 15:00–23:00 BJT transitions to the consumption phase ($-\partial W/\partial t>0$), with peak consumption rate around 18:00 BJT. The vertical velocity field maintains deep upward motion throughout the day, especially in the afternoon, extending from the surface to above 100 hPa, with the maximum ascent center near 400 hPa, reaching −0.13 Pa/s (Fig. 6i). The morning precipitation peak is directly driven by the strongly maintained dynamic convergence overnight, while the secondary afternoon peak, under the persistent dynamic convergence background, is promoted by diurnal solar radiation, further triggering convection through thermal lifting and releasing morning-accumulated energy, thus superimposing a thermally enhanced peak on the dynamic background. Additionally, the surface evaporation term is the weakest (Fig. 6b), likely related to suppression of surface energy budgets by persistent rainy weather.

The diversity of diurnal precipitation variations over the MLYRB stems from different combinations of physical processes. Morning precipitation days are mainly regulated by diurnal variations of large-scale dynamic forcing, with moisture sources primarily consuming pre-stored reserves; afternoon precipitation days are dominated by local thermal processes, relying on daytime moisture accumulation and energy storage; the dual-peak type results from combined effects of strong persistent dynamic forcing and diurnal

thermal forcing, where the morning peak mainly corresponds to the convergence maximum, while the afternoon peak reflects thermal processes modulating the persistent dynamic background.

3.3 Identification of spatial patterns in diurnal variation and corresponding configuration conditions

Building upon long-term observational datasets and employing spectral clustering methodology, this investigation systematically characterizes the regional differentiation of diurnal precipitation patterns, with particular emphasis on elucidating the diurnal variability of total PA. Traditional large-scale regional studies (Liu et al. 2021; Wu et al. 2018) typically identified only two to three precipitation regimes across the MLYRB: predominantly featuring either balanced bimodal or afternoon-dominant bimodal patterns, our analysis reveals four distinct patterns of PA diurnal variation. These patterns exhibit a progressive northwest-to-southeast transition (Fig. 7a, b), providing substantially refined spatial differentiation.

From Fig. 7a and b, the northwestern sector demonstrates a characteristic early-morning dominant regime (Pattern 2), where PA peaks distinctly (>0.27 mm/h) around 07:00 BJT. Notably, this region exhibits a very prominent peak in PF during the early morning, while the diurnal variation in PI is relatively mild (Fig. 7h, l). This indicates that the morning peak in this region is primarily due to a higher frequency of precipitation events. The transitional zone between the northwestern and southeastern regions (Pattern 1) exhibits a unique bimodal quasi-equilibrium structure, with comparable peaks in the early morning (~0.29 mm/h) and afternoon (~0.33 mm/h). PF and PI also exhibit similar diurnal characteristics. In the areas with abrupt topographic transitions (Pattern 4), particularly along the foothills of the Dabie, Huangshan, Mufu, and Jiuling Mountains, the afternoon PA peak intensifies markedly to 0.43 mm/h. The southeastern coastal region (Pattern 3) manifests the most pronounced diurnal amplitude, with PA reaching its maximum (~0.47 mm/h) in the afternoon. Unlike other regions, long-duration precipitation in this area does not exhibit a morning peak; instead, the afternoon peak is slightly higher than the morning peak (Fig. 7o).

It is particularly noteworthy that the transitional bimodal quasi-equilibrium (Pattern 1) and foothill afternoon enhanced (Pattern 4) PA diurnal variation patterns for the total precipitation exhibit independent differentiation in central regions, this feature has not been identified in previous studies. Further analysis indicates that the differences between Pattern 1 and Pattern 4 are mainly driven by afternoon precipitation (medium- and short-duration). Pattern 1 exhibits an earlier peak timing, and a higher peak value (Fig. 7p, q). As a typical representative of terrain-sensitive precipitation, Pattern 4 has a spatial distribution that closely matches the abrupt changes in elevation gradient.

The primary differences among the four precipitation patterns are predominantly manifested in their afternoon precipitation characteristics (Fig. 7o–q). Notably, the long-duration precipitation in Pattern 3 exhibits unique properties, with its morning peak not only being less pronounced but even slightly lower than the afternoon peak (Fig. 7o). The relatively uniform distribution of CAPE across the study region (Fig. 8f) rules out the dominance of local thermal instability; instead, the spatial differentiation patterns can be primarily attributed to secondary circulations driven by thermal contrasts such as mountain-plain and land-sea differential heating.

Specifically, the formation mechanism of Pattern 4 originates from mountain-plain thermal differences: daytime thermal contrast generates upward motion that superimposes with orographic forcing, manifesting as significantly enhanced afternoon ascent in the vertical velocity field (Fig. 8i), corresponding to an earlier intensification of MFC (Fig. 8a–c). In contrast, the distinctive features of Pattern 3 are attributed to land-sea thermal contrast: warm, moist air from the ocean advances landward and encounters dynamic lifting by the southeastern hills, with both processes synergistically forming strong convergent ascent (Fig. 8j). More detailed moisture budget decomposition reveals that MFC before the morning peak in this region primarily relies on the positive contribution from moisture advection (Fig. 8c), while the wind divergence term shows negative values (Fig. 8b). Conversely, the strong MFC preceding the afternoon peak results from combined contributions of both wind divergence and moisture advection terms (Fig. 8b, c), with the former being dominant. This finding suggests that during morning hours, moisture convergence is driven more by advective transport in the humidity field rather than pure wind field convergence. It is important to emphasize that although both patterns ultimately manifest as dynamic lifting, their initial driving mechanisms can be traced back to secondary circulations generated by thermal contrasts.

In the Pattern 1 region, the persistently convergent moisture flux (Fig. 8a–c) combined with moderate vertical motion throughout the day (Fig. 8g) shapes the distinctive bimodal structure. The Pattern 2 region exhibits a unique diurnal alternation in MFC characteristics (Fig. 8a–c). The transition to divergent conditions during 12:00–19:00 BJT in this region establishes a stable main morning precipitation peak, supported by the vertical velocity structure shown in Fig. 8h, which displays a well-defined morning ascent maximum.

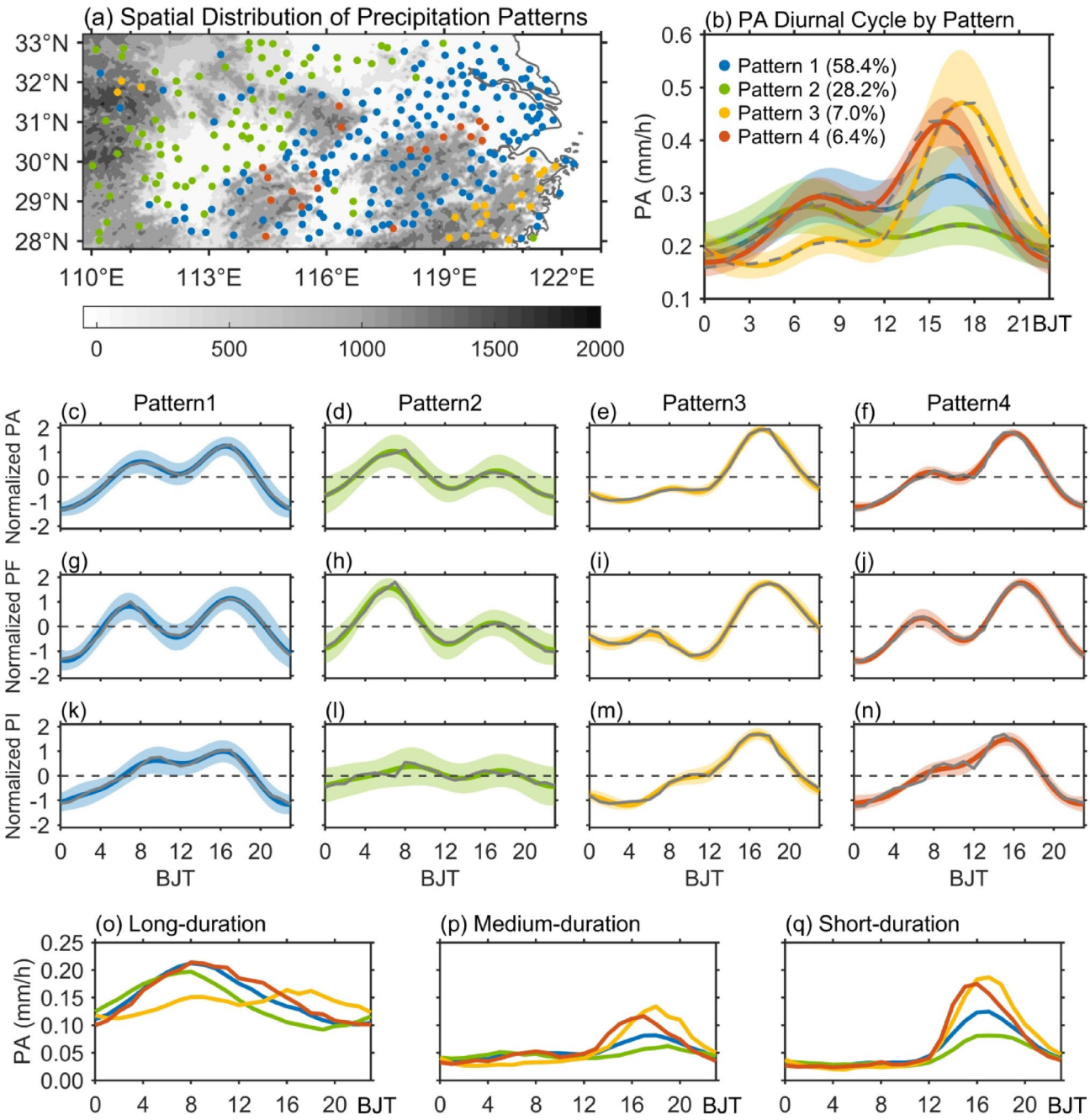

Fig. 7 Spatial distributions of summer PA patterns (**a**) and corresponding diurnal cycles (**b**) in the MLYRB averaged over 1980–2022, with shadings indicating the standard deviation among stations within each cluster. All diurnal cycles are derived using Fourier harmonic analysis, with the first three harmonics explaining most of the total daily variance. Normalized diurnal cycles of PA (**c**–**f**), PF(**g**–**j**), and PI (**k**–**n**) for the four identified patterns, diurnal variations of PA for long-duration (**o**), medium-duration (**p**), and short-duration (**q**) precipitation across the four patterns

The lagging characteristics of morning peaks from northwest to southeast observed in Fig. 7b and o, combined with the northwest-southeast oriented zonal distribution of the four precipitation patterns identified in this study, collectively suggest the potential existence of an organized diurnal propagation of precipitation in this region. Focusing on the propagation characteristics of PA diurnal peaks, a previously unrecognized distinct southeastward propagation of PA morning peaks within the 110°E-119°E, 28°N-30°N region is identified in this study (Fig. 9a, d) building upon existing research (Bao et al. 2011; Wu et al. 2018). Specifically, the northwest-southeastward lag of morning peaks of PA for the total precipitation closely corresponds to the propagation characteristics of long-duration precipitation (Fig. 9d, h)

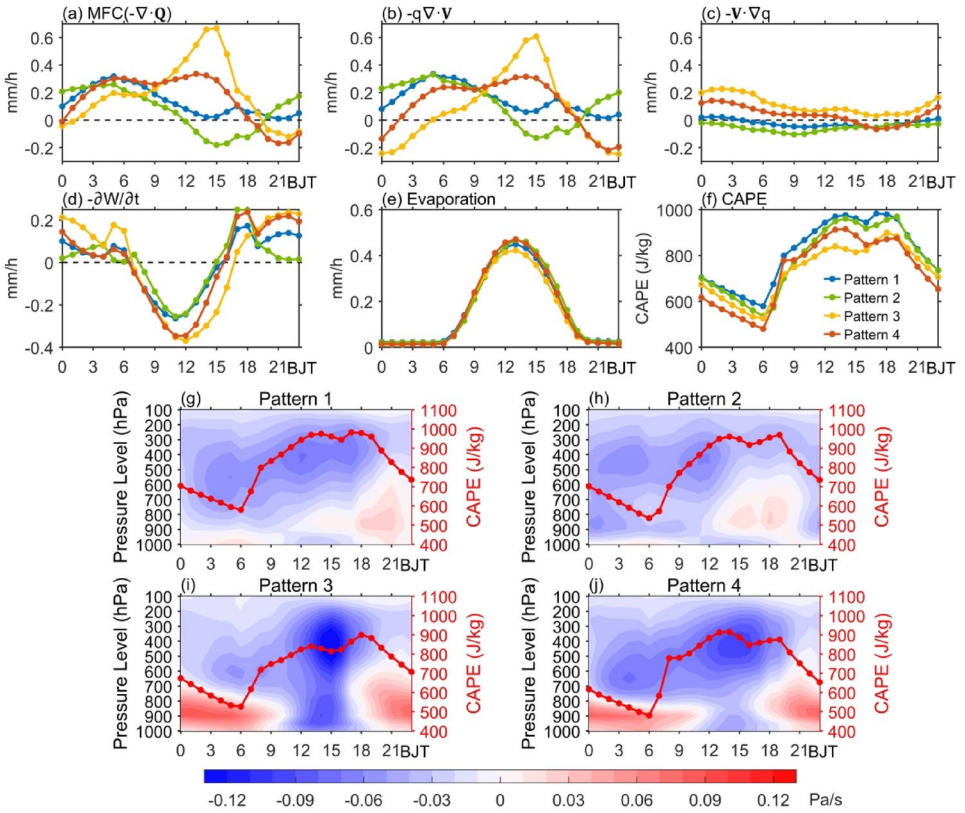

Fig. 8 Moisture budget components and atmospheric dynamic-thermodynamic characteristics for the four patterns of summer precipitation diurnal variation in the MLYRB: Diurnal variations of MFC ($-\nabla \cdot \vec{Q}$) (**a**), wind divergence term ($-q\nabla \cdot \vec{V}$) (**b**), moisture advection term ($-\vec{V} \cdot \nabla q$) (**c**), precipitable water tendency ($-\partial W/\partial t$) (**d**), evaporation (**e**), and CAPE (**f**); vertical velocity profiles with CAPE overlay (**g**–**j**)

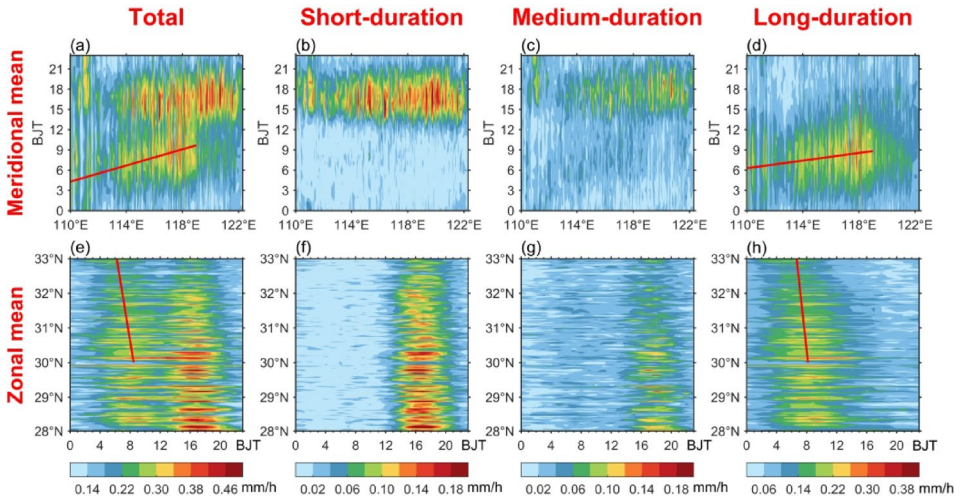

Fig. 9 Diurnal variations of PA for the total, short-, medium-, and long-duration precipitation in the MLYRB averaged over the summers of 1980–2022 regionally averaged along 28°N-33°N (**a**–**c**) and 110°E-122°E (**d**–**f**), respectively. The red lines indicate the delay of the diurnal peak time for the PA in the early morning

influenced by large-scale weather systems (the westerly jet stream and WPSH), while the localized (non-propagating) nature of afternoon peaks is predominantly associated with short-duration precipitation (Fig. 9b, e) that shows stronger dependence on convective activity.

3.4 Sub-seasonal characteristics of diurnal precipitation variations

The diurnal variation of summer precipitation in eastern China exhibits pronounced sub-seasonal heterogeneity (Yu et al. 2014). Based on the characteristics of our research data (Fig. 10d–f) and previous studies (Bao et al. 2011), the summer season is divided into three distinct periods: the pre-Meiyu phase (Pentads 31–33, June 1–15), the typical Meiyu period (Pentads 34–39, June 16-July 15), and the post-Meiyu phase (Pentads 40–48, July 16-August 31).

During the pre-Meiyu period, PA exhibits a characteristic south-high-north-low distribution, with the maximum moisture convergence center located in the southern part (Fig. 10a). As the Meiyu period begins, the PA distribution transitions to a northwest-low-southeast-high pattern,

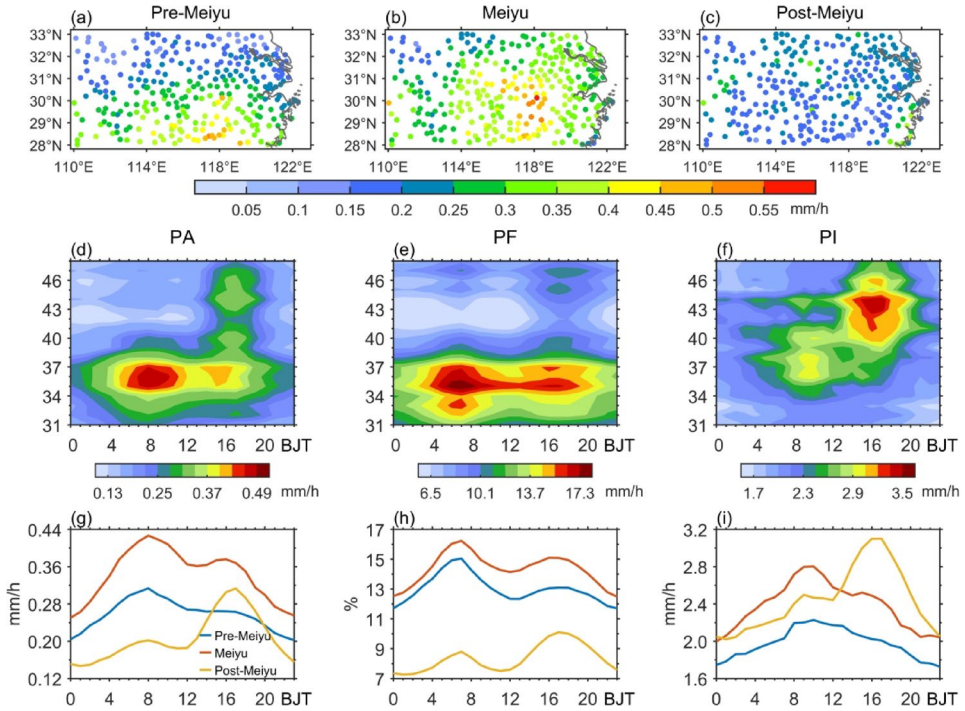

Fig. 10 Spatial distributions of the climatic mean PA (mm/h) during the pre-Meiyu (**a**), Meiyu (**b**), and post-Meiyu (**c**) periods in summers of 1980–2022. Sub-seasonal evolution of diurnal variations for the regional mean PA (**d**), PF(**e**), and PI (**f**) in the MLYRB, and the diurnal variations of PA (**g**), PF (**h**), and PI (**i**) regionally averaged over the MLYRB during pre-Meiyu, Meiyu, and post-Meiyu periods

particularly forming a pronounced precipitation center in the central MLYRB (Fig. 10b). By the post-Meiyu period, PA shows a notable decrease across the entire region (Fig. 10c). Among the 3 periods, precipitation in the Meiyu period demonstrates the most distinctive characteristics, with both PA and PF reaching their maxima (Fig. 10d, e) and exhibiting a stable bimodal diurnal pattern (Fig. 10g, h). Although both PI and PF in the pre-Meiyu period maintain similar bimodal structure, the intensities are relatively much weaker (Fig. 10h, i). During the post-Meiyu period, PI increases markedly (Fig. 10i) but PF decreases overall (Fig. 10h), resulting in a new bimodal structure with a primary afternoon peak and secondary morning peak (Fig. 10g). The consistently highest PA in the Meiyu period (Fig. 10d) originates from dual factors: PF maintains the highest values at each hour of the day (Fig. 10h), while PI demonstrates significant superiority from nighttime to noon (Fig. 10i). In contrast, the post-Meiyu period is characterized by "low total amount but prominent afternoon peak" (Fig. 10g) due to persistently low PF (Fig. 10h) values despite strong afternoon PI (Fig. 10i).

To elucidate the sub-seasonal modulation of precipitation diurnal variations by precipitation events with different duration, Fig. 11 further shows that the contribution of long-duration precipitation to total precipitation hours (total PA) shows a slightly increasing change during the pre-Meiyu period, exceeding 55% (70%) by the 30th pentad. Interestingly, during the Meiyu period, the contribution of long-duration precipitation steadily decreases, while that of the short-duration precipitation continues to rise. This transition demonstrates that although Meiyu precipitation in the MLYRB is predominantly stratiform and most frequent in the early morning (Zhang et al. 2022, 2020), the accumulation and release of local convective instability enhances atmospheric convection, making convective precipitation events more frequent or intense during the Meiyu period compared to the pre-Meiyu period, thereby forming the characteristic bimodal diurnal pattern.

In the post-Meiyu period (starting from the 40th pentad), long-duration precipitation still dominates PA contribution (Fig. 11b), but its contribution to precipitation hours rapidly decreases and is balanced by short-duration precipitation (each around 38%) (Fig. 11a). By the 44th pentad, their contributions stabilize, showing comparable precipitation hours but significantly greater PA contribution from long-duration precipitation. This evolutionary process reveals the dynamic interplay between stratiform and convective precipitation systems throughout the sub-seasonal progression, ultimately shaping the phased characteristics of summer precipitation diurnal variations.

The spatiotemporal evolution of precipitation characteristics from the pre-Meiyu to post-Meiyu periods is governed by a dynamic balance among moisture transport, dynamic forcing, and thermodynamic instability. Quantitative moisture budget analysis further reveals that both evaporation and the local precipitable water tendency term exhibit relatively limited variability throughout the summer (Fig. 12d, e). Differences in moisture conditions among the three periods are primarily driven by MFC, which is mainly reflected in changes in the wind divergence term (Fig. 12a–c).

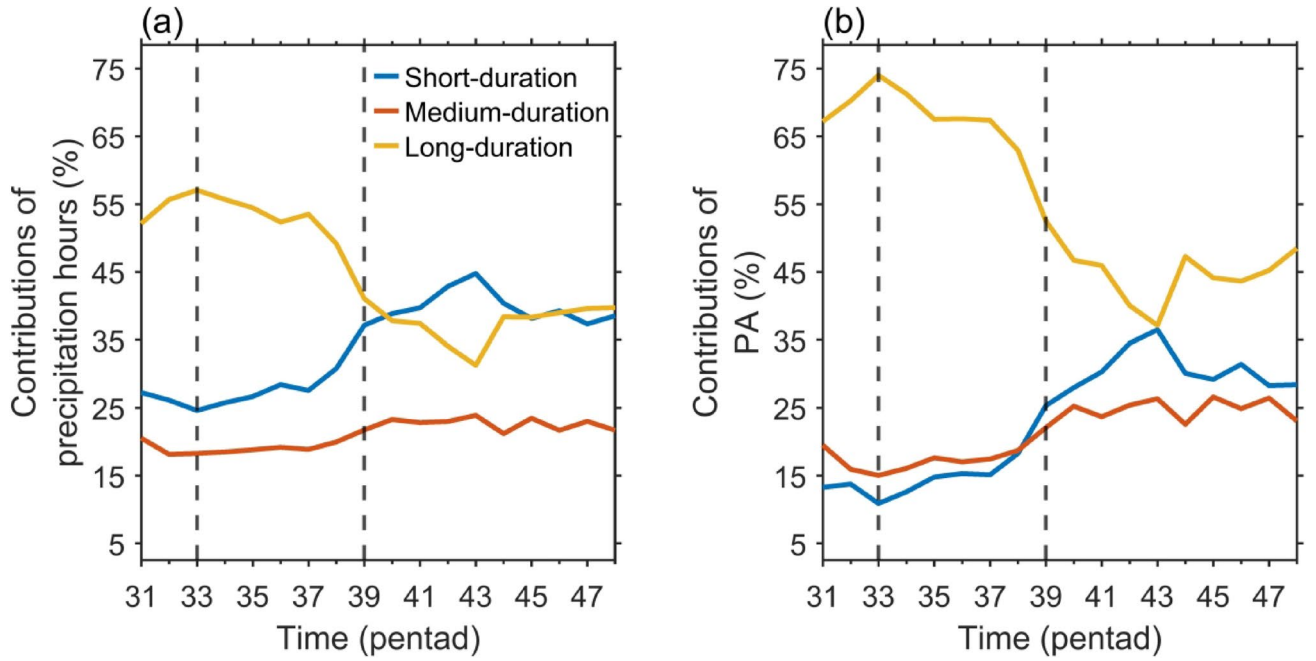

Fig. 11 Sub-seasonal variations in the contributions of precipitation events with different duration to the total precipitation in the MLYRB during the summers of 1980 to 2022, depicted by precipitation hours (**a**) and PA (**b**). The dashed lines (33th and 39th pentad) divide the three periods: the pre-Meiyu period, the Meiyu period, and the post-Meiyu period

As the Meiyu period commences, the intensification of the southwesterly monsoon leads to a peak in both dynamic and moisture conditions. This is evidenced by the strongest MFC (Fig. 12a, h) and upward motion (Fig. 12k) among all periods. This powerful dynamic lifting, working in concert with abundant moisture, is the key driver for the highest PA and PF, forming a pronounced precipitation center in the central MLYRB and establishing a stable bimodal diurnal pattern. The morning peak is triggered by the maximum nocturnal MFC and large-scale upward motion, while the afternoon peak is supported by the diurnal development of thermodynamic instability alongside residual dynamic forcing.

In contrast, the post-Meiyu period is characterized by a fundamental shift in the governing mechanisms. The significant weakening of southwesterly moisture transport leads to a marked decrease in MFC (Fig. 12a, i) and overall PF, resulting in a notable reduction of PA across the region. However, thermodynamic conditions become dominant, with CAPE reaching its maximum, particularly in the afternoon (Fig. 12l). This strong instability drives intense afternoon convection. Consequently, the precipitation regime transitions to a "low total amount but prominent afternoon peak" pattern, where high PI) cannot fully compensate for the low PF, yielding a new bimodal structure with a primary afternoon peak.

4 Summary and discussion

This study comprehensively investigates the diurnal variation characteristics of summer precipitation over the MLYRB and associated mechanisms using high-resolution hourly rain gauge data and ERA5 reanalyses data during1980 to 2022. The results reveal a distinct bimodal diurnal cycle in precipitation, with primary peaks occurring in the early morning (07:00–09:00 BJT) and late afternoon (16:00–18:00 BJT). The morning peak is predominantly driven by the long-duration precipitation events associated with enhanced nocturnal moisture transport and large-scale convergence, while the afternoon peak is mainly attributed to the short-duration precipitation triggered by solar heating and local thermal instability.

Through composite analysis of the three types of regional rainy day, this study reveals their fundamentally different environmental configurations. The morning-type precipitation days exhibit typical "nocturnal convergence-daytime divergence" moisture conditions and "moisture consumption" characteristics, primarily driven by nocturnal large-scale dynamic lifting mechanisms that consume pre-stored moisture, while thermal conditions remain relatively stable. The afternoon-type precipitation days show "persistent weak convergence" and "moisture storage-release" features, dominated by local thermal processes and relying on daytime surface evaporation and energy storage. The dual-peak type precipitation days demonstrate more complex

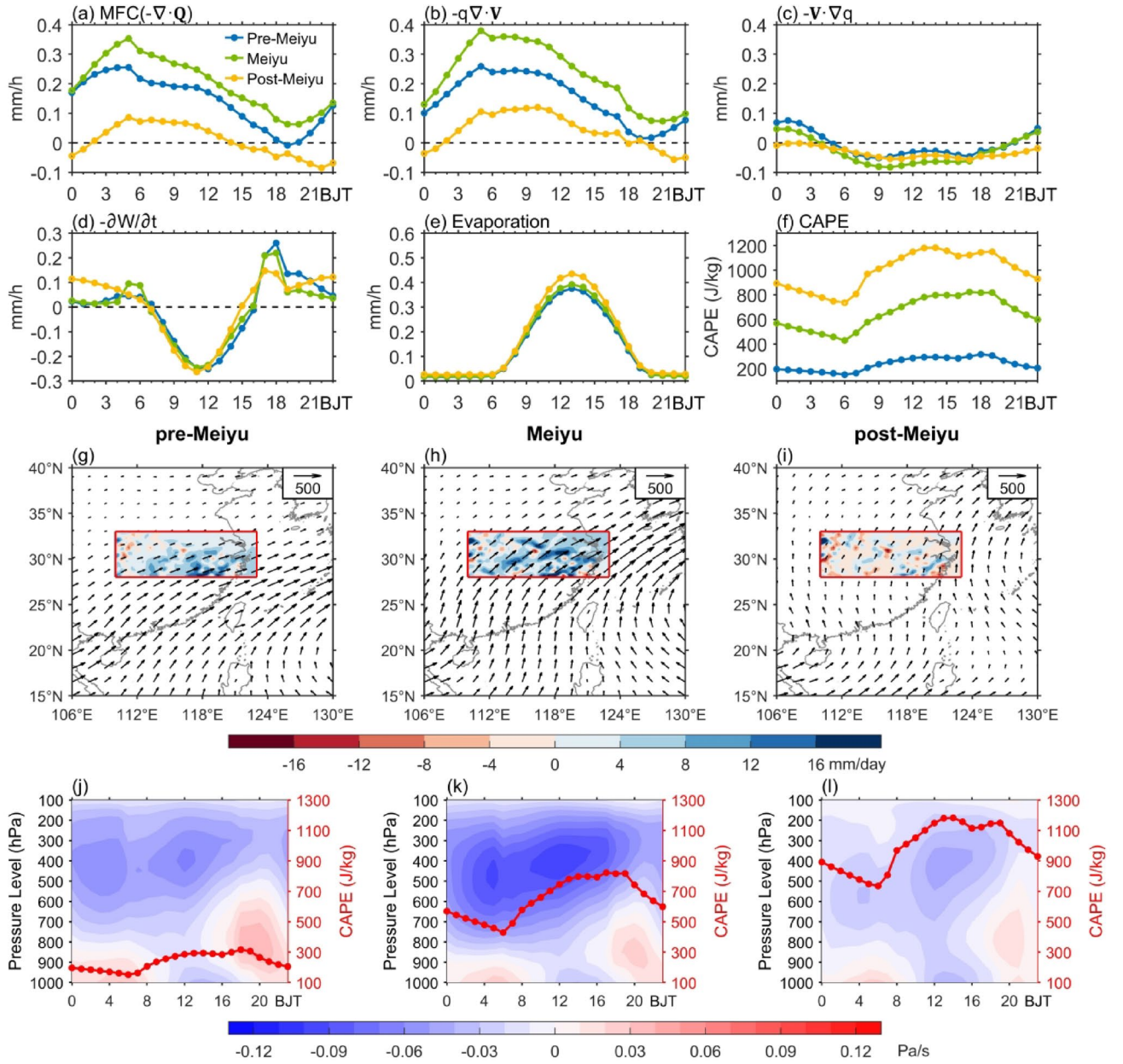

Fig. 12 Moisture budget components and atmospheric dynamic-thermodynamic characteristics for the three periods in the MLYRB: Diurnal variations of MFC ($-\nabla \cdot \vec{Q}$) (**a**), wind divergence term ($-q\nabla \cdot \vec{V}$) (**b**), moisture advection term ($-\vec{V} \cdot \nabla q$) (**c**), precipitable water tendency ($-\partial W/\partial t$) (**d**), evaporation (**e**), and CAPE (**f**); Column-integrated (surface to 100 hPa) moisture flux (vectors, kg m^{-1} s^{-1}) and its convergence (MFC, shading, mm/day) for pre-Meiyu (**d**), Meiyu (**e**), and post-Meiyu (**f**) periods; vertical velocity profiles with CAPE overlay for pre-Meiyu (**j**), Meiyu (**k**), and post-Meiyu (**l**) periods

"strong convergence" and "semi-diurnal cycle" characteristics, where the morning peak is directly driven by persistent dynamic convergence, and the afternoon peak is formed through thermal lifting that releases energy accumulated in the morning under the persistent dynamic background, reflecting synergy between dynamic forcing and thermal processes.

Spatially, four distinct precipitation diurnal variation patterns are identified through spectral clustering: a transitional bimodal equilibrium pattern, an early-morning dominant regime in the northwest, an afternoon-enhanced pattern along mountainous foothills, and a strong afternoon peak in the southeastern coastal region. The transitional bimodal equilibrium pattern (Pattern 1) is maintained through persistent moisture convergence combined with moderate vertical ascending motion; the northwestern morning-dominant pattern (Pattern 2) is controlled by large-scale dynamic processes, with its daytime moisture divergence characteristics

favoring the stable development of main morning peaks; the southeastern coastal afternoon-enhanced pattern (Pattern 3) is driven by land-sea thermal contrasts, where warm moist air from the ocean undergoes topographic lifting by southeastern hills to form strong convergent ascent; while the mountainous afternoon-enhanced pattern (Pattern 4) is triggered by mountain-plain thermal differences, with orographic lifting further amplifying afternoon vertical ascent. In addition, a southeastward delay in the early-morning precipitation peak is observed within the 110°E-119°E, 28°N-30°N domain, extending previous findings on eastward propagation that were limited to areas west of 114°E (Bao et al. 2011; Wu et al. 2018).

The sub-seasonal analysis further highlights the dynamic evolution of precipitation diurnal cycles, transitioning from a morning-dominated regime during the pre-Meiyu and Meiyu periods to an afternoon-dominated regime in the post-Meiyu period. This evolution is closely linked to the shifting balance between large-scale moisture transport and convective instability, with quantitative moisture budget analysis revealing that differences across periods mainly stem from variations in MFC, particularly the wind divergence term, rather than evaporation or local precipitable water changes. The Meiyu period exhibits optimal moisture conditions with the strongest MFC and robust upward motion, while the post-Meiyu period is characterized by weakened dynamic forcing but enhanced thermodynamic instability.

Despite in-depth analyses of the fine-scale characteristics of multi-year average summer precipitation diurnal variation, a comprehensive understanding of the causes of diurnal variability is still limited. Future research should employ higher-resolution data and numerical simulation methods to further explore the impacts of complex terrain, monsoon climate, and urban heat island effects on precipitation diurnal variation, aiming to elucidate the underlying physical mechanisms.

Acknowledgements This study is supported by the National Natural Science Foundation of China under Grants U2342207, the Postgraduate Research and Practice Innovation Program of Jiangsu Province (No. 206 in 2024), and the Jiangsu Collaborative Innovation Center for Climate Change, and the Science and Technology Talents and Platform Plan: Technology Innovation Center of Yunnan Province for Digital Water Engineering (No. 202305AK34003).

Author contributions X Y carried out data analysis and wrote the initial draft of manuscript. X Y, A H, D X and S Z interpreted the results and improved the writing. All authors made contributions to the draft, read and approved the final manuscript.

Funding This study is funded by the National Natural Science Foundation of China under Grants U2342207, the Postgraduate Research and Practice Innovation Program of Jiangsu Province (No. 206 in 2024), and the Jiangsu Collaborative Innovation Center for Climate Change.

Data availability The hourly rain gauge precipitation provided by the China Meteorological Administration. The other hourly meteorological data obtained from ECMWF Reanalysis v5 (ERA5) is available at https://cds.climate.copernicus.eu/datasets/reanalysis-era5-pressure-levels.

Declarations

Competing Interests The authors have no relevant financial or non-financial interests to disclose.

References

Bao XH, Zhang FQ, Sun JH (2011) Diurnal variations of warm-season precipitation east of the Tibetan Plateau over China. Mon Weather Rev 139(9):2790–2810. https://doi.org/10.1175/mwr-d-11-00006.1

Calinski T, Harabasz J (1974) A dendrite method for cluster analysis: communications in statistics. Theor Method 3(1):1–27. https://doi.org/10.1080/03610927408827101

Chen GX, Sha WM, Iwasaki T (2009a) Diurnal variation of precipitation over southeastern China: spatial distribution and its seasonality. J Geophys Res Atmos 114:D13103. https://doi.org/10.1029/2008jd011103

Chen GX, Sha WM, Iwasaki T (2009b) Diurnal variation of precipitation over southeastern China: 2. Impact of the diurnal monsoon variability. J Geophys Res Atmos 114:D21105. https://doi.org/10.1029/2009jd012181

Chen HM, Yu RC, Li J, Yuan WH, Zhou TJ (2010) Why nocturnal long-duration rainfall presents an eastward-delayed diurnal phase of rainfall down the Yangtze River Valley. J Climate 23(4):905–917. https://doi.org/10.1175/2009jcli3187.1

Chen GX, Sha WM, Iwasaki T, Ueno K (2012) Diurnal variation of rainfall in the Yangtze River Valley during the spring-summer transition from TRMM measurements. J Geophys Res Atmos 117:D06106. https://doi.org/10.1029/2011jd017056

Chen HM, Yu RC, Shen Y (2016) A new method to compare hourly rainfall between station observations and satellite products over Central-Eastern China. J Meteorol Res 30(5):737–757. https://doi.org/10.1007/s13351-016-6002-5

Chen GX, Lan RY, Zeng WX, Pan H, Li WB (2018) Diurnal variations of rainfall in surface and satellite observations at the monsoon coast (South China). J Climate 31(5):1703–1724. https://doi.org/10.1175/jcli-d-17-0373.1

Dai Z, Yu R, Li J, Chen H (2011) The characteristics of summer precipitation diurnal variations in three reanalysis datasets over China. Meteorol Monthly 37(1):21–30

Fu PL, Zhu KF, Zhao K, Zhou BW, Xue M (2019) Role of the nocturnal low-level jet in the formation of the morning precipitation peak over the Dabie Mountains. Adv Atmos Sci 36(1):15–28. https://doi.org/10.1007/s00376-018-8095-5

Geng B, Yamada H (2007) Diurnal variations of the Meiyu/Baiu rain belt. Sola 3:61–64. https://doi.org/10.2151/sola.2007-016

Geng BO, Yamada H, Reddy KK, Uyeda H, Fujiyoshi Y (2009) Mesoscale development and along-frontal variation of a Meiyu/Baiu front and precipitation observed in the downstream region of the Yangtze River. J Meteorol Soc Jpn 87(3):423–457. https://doi.org/10.2151/jmsj.87.423

Hansen J, Sato M, Ruedy R (2012) Perception of climate change. Proc Natl Acad Sci U S A 109(37):E2415–E2423. https://doi.org/10.1073/pnas.1205276109

He ZW, Zhang QH, Sun J (2016) The contribution of mesoscale convective systems to intense hourly precipitation events

during the warm seasons over central East China. Adv Atmos Sci 33(11):1233–1239. https://doi.org/10.1007/s00376-016-6034-x
Held IM, Soden BJ (2006) Robust responses of the hydrological cycle to global warming. J Climate 19(21):5686–5699. https://doi.org/10.1175/jcli3990.1
Hersbach H, Bell B, Berrisford P, Hirahara S, Horányi A, Muñoz-Sabater J, Nicolas J, Peubey C et al (2020) The ERA5 global reanalysis. Q J R Meteorol Soc 146(730):1999–2049. https://doi.org/10.1002/qj.3803
Hu Y, Deng Y, Zhou ZM, Cui CG, Dong XQ (2019) A statistical and dynamical characterization of large-scale circulation patterns associated with summer extreme precipitation over the middle reaches of Yangtze river. Clim Dyn 52(9–10):6213–6228. https://doi.org/10.1007/s00382-018-4501-z
Huang WR, Wang SYS (2017) Future changes in propagating and non-propagating diurnal rainfall over East Asia. Clim Dyn 49(1–2):375–389. https://doi.org/10.1007/s00382-016-3348-4
Hur J, Raghavan SV, Nguyen NS, Liong SY (2018) Are satellite products good proxies for gauge precipitation over Singapore? Theor Appl Climatol 132(3–4):921–932. https://doi.org/10.1007/s00704-017-2132-7
Jiang ZY, Liu DQ, Dong GT, Tang JP, Wang SG, Xiong YT (2024) Convection-permitting regional climate simulations over coastal regions in China. Clim Dyn 62(8):7271–7291. https://doi.org/10.1007/s00382-024-07278-z
Jin EK, Choi IJ, Kim SY, Han JY (2016) Impact of model resolution on the simulation of diurnal variations of precipitation over East Asia. J Geophys Res Atmos 121(4):1652–1670. https://doi.org/10.1002/2015jd023948
Li RZ, Wang KC, Qi D (2018) Validating the integrated multisatellite retrievals for global precipitation measurement in terms of diurnal variability with hourly gauge observations collected at 50,000 stations in China. J Geophys Res Atmos 123(18):10423–10442. https://doi.org/10.1029/2018jd028991
Li J, Chen HM, Li PX, Jiang XW (2023) Evaluating the precipitation biases over the western periphery of the Sichuan Basin with the ECMWF operational forecast model. Weather Forecast 38(8):1481–1496. https://doi.org/10.1175/waf-d-22-0218.1
Li J, Chen HM, Jiang XW, Li PX (2024) Diurnal variations of summer rainfall response to large-scale circulations and low-level winds over the Sichuan Basin. Clim Dyn 62(3):2041–2056. https://doi.org/10.1007/s00382-023-07009-w
Liu JZ, Yang L, Jiang JC, Yuan WH, Duan Z (2021) Mapping diurnal cycles of precipitation over China through clustering. J Hydrol 592:125804. https://doi.org/10.1016/j.jhydrol.2020.125804
Liu W, Lü HS, Zhu YH, Wang XY, Gao P, Su JB (2024) The performance of IMERG near-real-time estimations during the record-breaking Meiyu season in 2020. J Hydrol 634:131024. https://doi.org/10.1016/j.jhydrol.2024.131024
Lu E, Zhao W, Zou XK, Ye DX, Zhao CY, Zhang Q (2017) Temporal-spatial monitoring of an extreme precipitation event: determining simultaneously the time period it lasts and the geographic region it affects. J Climate 30(16):6123–6132. https://doi.org/10.1175/jcli-d-17-0105.1
Mao JY, Wu GX (2012) Diurnal variations of summer precipitation over the Asian monsoon region as revealed by TRMM satellite data. Sci China Earth Sci 55(4):554–566. https://doi.org/10.1007/s11430-011-4315-x
Meehl GA, Zwiers F, Evans J, Knutson T, Mearns L, Whetton P (2000) Trends in extreme weather and climate events: issues related to modeling extremes in projections of future climate change. Bull Am Meteorol Soc 81(3):427–436. https://doi.org/10.1175/1520-0477(2000)081%3c0427:Tiewac%3e2.3.CO;2
Ng AY, Jordan MI, Weiss Y (2001) On spectral clustering: analysis and an algorithm. In: 15th annual conference on neural information processing systems (NIPS) (Vol. 14: pp. 849–856) Vancouver, Canada
Niu XR, Tang JP, Wang SY, Fu CB, Chen DL (2020) On the sensitivity of seasonal and diurnal precipitation to cumulus parameterization over CORDEX-EA-II. Clim Dyn 54(1–2):373–393. https://doi.org/10.1007/s00382-019-05010-w
Oki T, Kanae S (2006) Global hydrological cycles and world water resources. Science 313(5790):1068–1072. https://doi.org/10.1126/science.1128845
Qian TT, Zhao P, Zhang FQ, Bao XH (2015) Rainy-season precipitation over the Sichuan Basin and adjacent regions in southwestern China. Mon Weather Rev 143(1):383–394. https://doi.org/10.1175/mwr-d-13-00158.1
Qin S, Wang KC, Wu GC, Ma ZS (2021) Variability of hourly precipitation during the warm season over eastern China using gauge observations and ERA5. Atmos Res 264:105872. https://doi.org/10.1016/j.atmosres.2021.105872
Rodell M, Famiglietti JS, Wiese DN, Reager JT, Beaudoing HK, Landerer FW, Lo MH (2018) Emerging trends in global freshwater availability. Nature 557(7707):650. https://doi.org/10.1038/s41586-018-0123-1
Shen Y, Xiong AY, Wang Y, Xie PP (2010) Performance of high-resolution satellite precipitation products over China. J Geophys Res Atmos 115:D02114. https://doi.org/10.1029/2009jd012097
Shi JB, Malik J (2000) Normalized cuts and image segmentation. IEEE Trans Pattern Anal Mach Intell 22(8):888–905. https://doi.org/10.1109/34.868688
Shi WR, Zhu KF, Li X, Zhang B (2024) Evaluation of precipitation forecast by the operational China meteorological administration mesoscale model during the 2020 Meiyu period. J Geophys Res Atmos 129(11):e2023JD039156. https://doi.org/10.1029/2023jd039156
Singh P, Nakamura K (2009) Diurnal variation in summer precipitation over the central Tibetan Plateau. J Geophys Res Atmos 114:D20107. https://doi.org/10.1029/2009jd011788
Song YY, Wei JF (2021) Diurnal cycle of summer precipitation over the North China Plain and associated land-atmosphere interactions: evaluation of ERA5 and MERRA-2. Int J Climatol 41(13):6031–6046. https://doi.org/10.1002/joc.7166
Tang GQ, Clark MP, Papalexiou SM, Ma ZQ, Hong Y (2020) Have satellite precipitation products improved over last two decades? A comprehensive comparison of GPM IMERG with nine satellite and reanalysis datasets. Remote Sens Environ 240:111697. https://doi.org/10.1016/j.rse.2020.111697
Tang Y, Huang AN, Wu PL, Huang DQ, Xue DK, Wu Y (2021) Drivers of summer extreme precipitation events over East China. Geophys Res Lett 48(11):e2021GL093670. https://doi.org/10.1029/2021gl093670
Trenberth KE (1991) Climate diagnostics from global analyses: conservation of mass in ECMWF analyses. J Climate 4(7):707–722. https://doi.org/10.1175/1520-0442(1991)004%3c0707:Cdfgac%3e2.0.Co;2
Trenberth KE, Dai A, Rasmussen RM, Parsons DB (2003) The changing character of precipitation. Bull Am Meteorol Soc 84(9):1205–1217. https://doi.org/10.1175/bams-84-9-1205
Trenberth KE, Smith L, Qian TT, Dai A, Fasullo J (2007) Estimates of the global water budget and its annual cycle using observational and model data. J Hydrometeorol 8(4):758–769. https://doi.org/10.1175/jhm600.1
Tucker DF (1993) Diurnal precipitation variations in south-central New-Mexico. Mon Weather Rev 121(7):1979–1991
von Luxburg U (2007) A tutorial on spectral clustering. Stat Comput 17(4):395–416. https://doi.org/10.1007/s11222-007-9033-z
Watters D, Battaglia A (2019) The summertime diurnal cycle of precipitation derived from IMERG. Remote Sens 11(15):1781. https://doi.org/10.3390/rs11151781

Wu Y, Huang AN, Huang DQ, Chen F, Yang B, Zhou Y, Fang DX, Zhang LJ et al (2018) Diurnal variations of summer precipitation over the regions east to Tibetan Plateau. Clim Dyn 51(11–12):4287–4307. https://doi.org/10.1007/s00382-017-4042-x

Xiao C, Wu PL, Zhang LX, Song LC (2016) Robust increase in extreme summer rainfall intensity during the past four decades observed in China. Sci Rep 6:38506. https://doi.org/10.1038/srep38506

Xuan SL, Zhang QY, Sun SQ, Shi CL (2018) Contrast in the East Asian subtropical westerly jet and its association with precipitation in China between early summer and midsummer. Meteorol Appl 25(1):119–127. https://doi.org/10.1002/met.1675

Xue M, Luo X, Zhu KF, Sun ZQ, Fei JF (2018) The controlling role of boundary layer inertial oscillations in Meiyu frontal precipitation and its diurnal cycles over China. J Geophys Res Atmos 123(10):5090–5115. https://doi.org/10.1029/2018jd028368

Yang RY, Zhang YC, Sun JH, Li J (2020) The comparison of statistical features and synoptic circulations between the eastward-propagating and quasi-stationary MCSs during the warm season around the second-step terrain along the middle reaches of the Yangtze River. Science China-Earth Sciences 63(8):1209–1222. https://doi.org/10.1007/s11430-018-9385-3

Yin SQ, Chen DL, Xie Y (2009) Diurnal variations of precipitation during the warm season over China. Int J Climatol 29(8):1154–1170. https://doi.org/10.1002/joc.1758

Yu RC, Xu YP, Zhou TJ, Li J (2007a) Relation between rainfall duration and diurnal variation in the warm season precipitation over central eastern China. Geophys Res Lett 34(13):L13703. https://doi.org/10.1029/2007gl030315

Yu RC, Zhou TJ, Xiong AY, Zhu YJ, Li JM (2007b) Diurnal variations of summer precipitation over contiguous China. Geophys Res Lett 34(1):L01704. https://doi.org/10.1029/2006gl028129

Yu RC, Li J, Chen HM, Yuan WH (2014) Progress in studies of the precipitation diurnal variation over contiguous China. J Meteorol Res 28(5):877–902. https://doi.org/10.1007/s13351-014-3272-7

Yuan WH, Yu RC, Chen HM, Li JA, Zhang MH (2010) Subseasonal characteristics of diurnal variation in summer monsoon rainfall over central eastern China. J Climate 23(24):6684–6695. https://doi.org/10.1175/2010jcli3805.1

Yuan WH, Li J, Chen HM, Yu RC (2012a) Intercomparison of summer rainfall diurnal features between station rain gauge data and TRMM 3B42 product over central eastern China. Int J Climatol 32(11):1690–1696. https://doi.org/10.1002/joc.2384

Yuan WH, Yu RC, Zhang MH, Lin WY, Chen HM, Li J (2012b) Regimes of diurnal variation of summer rainfall over subtropical East Asia. J Climate 25(9):3307–3320. https://doi.org/10.1175/jcli-d-11-00288.1

Zeng JW, Huang AN, Wu PL, Huang DQ, Zhang Y, Tang J, Zhao DJ, Yang B et al (2023) Typical synoptic patterns responsible for summer regional hourly extreme precipitation events over the Middle and Lower Yangtze River Basin, China. Geophys Res Lett 50(17):e2023GL104829. https://doi.org/10.1029/2023gl104829

Zhang ZW (2022) Impact of typhoons of different intensities on short-term precipitation in the middle and lower reaches of the Yangtze River in Summer. Adv Meteorol 2022:6227798. https://doi.org/10.1155/2022/6227798

Zhang AQ, Chen YL, Zhou SN, Cui CG, Wan R, Fu YF (2020) Diurnal variation of Meiyu rainfall in the Yangtze Plain during atypical Meiyu years. J Geophys Res Atmos 125(1):e2019JD031742. https://doi.org/10.1029/2019jd031742

Zhang WX, Furtado K, Wu PL, Zhou TJ, Chadwick R, Marzin C, Rostron J, Sexton D (2021) Increasing precipitation variability on daily-to-multiyear time scales in a warmer world. Sci Adv 7(31):eabf8021. https://doi.org/10.1126/sciadv.abf8021

Zhang AQ, Chen YL, Zhou SN, Chen SM, Li WB (2022) Precipitation microphysics during the extreme Meiyu period in 2020. Remote Sens 14(7):1651. https://doi.org/10.3390/rs14071651

Zhao JH, Yang L, Gu BH, Yang J, Feng GL (2016) On the relationship between the winter Eurasian teleconnection pattern and the following summer precipitation over China. Adv Atmos Sci 33(6):743–752. https://doi.org/10.1007/s00376-015-5195-3

Zhou TJ, Yu RC, Chen HM, Dai A, Pan Y (2008) Summer precipitation frequency, intensity, and diurnal cycle over China: a comparison of satellite data with rain gauge observations. J Climate 21(16):3997–4010. https://doi.org/10.1175/2008jcli2028.1

Zhou ZQ, Xie SP, Zhang RH (2021) Historic Yangtze flooding of 2020 tied to extreme Indian Ocean conditions. Proc Natl Acad Sci USA 118(12):e2022255118. https://doi.org/10.1073/pnas.2022255118

Zhu LM, Liu JZ, Zhu AX, Sheng ML, Duan Z (2018) Spatial distribution of diurnal rainfall variation in summer over China. J Hydrometeorol 19(4):667–678. https://doi.org/10.1175/jhm-d-17-0176.1

Zhu SX, Liu CT, Cao J, Lavigne T (2023) Diurnal precipitation features over complex terrains along the Yangtze River in China based on long-term TRMM and GPM radar products. Remote Sens 15(13):3451. https://doi.org/10.3390/rs15133451